Acta Cryst. (1979). A35, 449–458

Intersecting Defect Structures in Gallia- and Magnesia-Doped Rutiles

BY L. A. BURSILL

School of Physics, The University of Melbourne, Parkville 3052, *Australia*

(*Received* 28 *August* 1978; *accepted* 11 *December* 1978)

Abstract

The possible $\{210\}\langle 0\frac{1}{2}0\rangle$ defect intersection structures of rutile are analysed. There are 41 distinct intersection classes, 26 of which may exist as enantiomorphic forms. A classification scheme is introduced and used to analyse 386 observed intersections. Examples of 25 classes occur; eight of these account for 87% of the observations. The occurrence frequency may be understood by analysis of the stair-rod dislocation Burger's vector, required for continuity of the rutile structure around the intersection. Structural models for the commonly observed intersections and the nature of the 'dislocation-core' structures are presented. Exceptionally large tunnels are generated at orthogonal intersections and some high-resolution images are discussed. Statistical analysis shows that the distribution over the possible classes is not random, suggesting that an equilibrium network of intersecting defects may arise after long reaction times. The stability and mobility of intersections is expected to determine the kinetics of the reaction between rutile and dopants. Intersection structures may act as nuclei for low- to high-temperature phase transformations and they may aggregate and order to form new ordered structures.

1. Introduction

The phases $Ga_4Ti_{m-4}O_{2m-1}$ ($15 \leq m \leq 23$, m odd) are derived from rutile by periodic repetition of (210) crystallographic shear planes (CSP) (Gibb & Anderson, 1972). The displacement vector $[0\frac{1}{2}0]$ was deduced using diffraction contrast analysis of isolated defects. Measurement of electron diffraction patterns from ordered CSP gave displacement vector $[\frac{1}{2}\frac{1}{4}\frac{1}{2}]$ (Bursill & Stone, 1975). This was confirmed by X-ray structural analysis of $Ga_4Ti_{21}O_{48}$ (Lloyd, Grey & Bursill, 1976). Columnar elements of the β-gallia structure, coherently intergrown with the rutile matrix, are separated along the CSP by relatively large tunnels having roughly hexagonal cross sections (Fig. 1*a*). The refinement showed that Ga^{3+} occupied the tetrahedral sites and 64% of the edge-shared octahedral sites at the CSP, with the remaining Ga^{3+} substituting for Ti^{4+} in the rutile slabs. Both the tunnels and the rutile matrix were imaged by high-resolution electron microscopy when it was found that isolated defects were in fact pairs of (210) $[\frac{1}{2}\frac{1}{4}\frac{1}{2}]$ CSP having stoichiometry Ga_4TiO_8 and overall displacement vector $[0\frac{1}{2}0]$ (Stone & Bursill, 1977; see Fig. 1*b*).

Analysis of the relations between rutile, β-gallia,

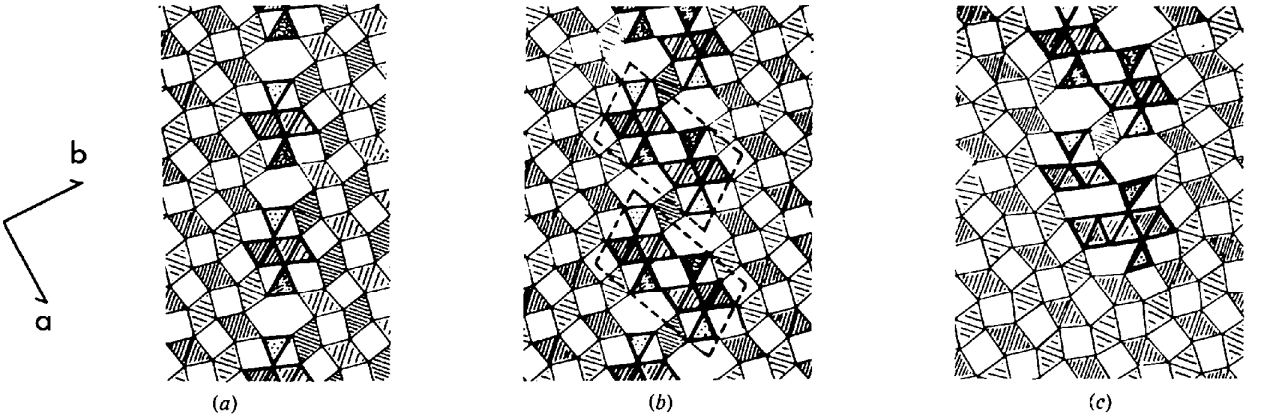

(*a*) (*b*) (*c*)

Fig. 1. (*a*) Structure of a (210)$[\frac{1}{2}\frac{1}{4}\frac{1}{2}]$ CSP in Ga-doped rutile. Note the β-gallia-type elements (thick lines) coherently intergrown with adjacent rutile slabs and the large tunnels having roughly hexagonal outlines. Octahedra share edges along the projection axis. (*b*) Structure of a (210)$[0\frac{1}{2}0]$ Ga_4TiO_8 defect-pair in rutile; larger β-gallia intergrowths are indicated. (*c*) Strip of triple edge-shared octahedra at dislocation core on termination of a defect-pair in rutile.

0567-7394/79/030449-10$01.00 © 1979 International Union of Crystallography

hollandite and the gallium titanate structure types shows that elements of the hollandite, psilomelane and new related tunnel structures arise naturally at the junction of orthogonal $(210)[\frac{111}{242}]$ and $(\bar{1}20)[\frac{111}{422}]$ CSP (Bursill, 1979*a*).

In this paper all of the possible $\{210\}\langle 0\frac{1}{2}0\rangle$ defect-pair intersection structures are derived and a statistical analysis is made of 386 observed intersections. An understanding of such intersection structures should lead to more predictable and controlled production of novel tunnel structures. In the following papers we describe the intergrowth of β-gallia, rutile and hollandite (Bursill & Stone, 1979*a*; Bursill, 1979*b*), other novel variations of the hollandite structure (Bursill & Netherway, 1979) and the intergrowth of ramsdellite (γ-MnO_2) with rutile, producing $\{100\}\langle\frac{111}{242}\rangle$ CSP (Bursill & Stone, 1979*b*).

2. Classification of intersecting defect structures

Application of the operations of the rutile space group $P4_2/mnm$ to a slab of rutile containing a Ga_4TiO_8 defect-pair generates the four crystallographically equivalent $\{210\}\langle 0\frac{1}{2}0\rangle$ structures given in Fig. 2(*a*,*b*,*c*,*d*). Vertical midplanes (dotted) contain only twofold symmetry axes parallel to the rutile *c* axis. The labelling scheme adopted in this paper, and its location relative to the rutile axes, is shown in Fig. 3. It is convenient to label a CSP as either $(hkl)[0\frac{1}{2}0]$ or $(\bar{h}\bar{k}\bar{l})[0\bar{\frac{1}{2}}0]$ to distinguish diametrically opposite sides of a junction. The angles between pairs of defects are listed in Table 1.

Given that there are eight possible positions for a defect-pair relative to a junction, that each position may be filled or empty, and neglecting the trivial case that there are no CSP, then there are $2^8 - 1 = 255$ possible junctions. This number is reduced to 41 crystallographically distinct structures by symmetry considerations. In most cases the symmetry factor is 4, corresponding to operation of the 4_2 screw axis (4 in

Table 1. *Angles between pairs of* $\{210\}$ *planes of rutile*

	$2\bar{1}0$	120	$\bar{1}20$
210	53·13°	36·87°	90·00°
$2\bar{1}0$		90·00	143·13
120			126·87

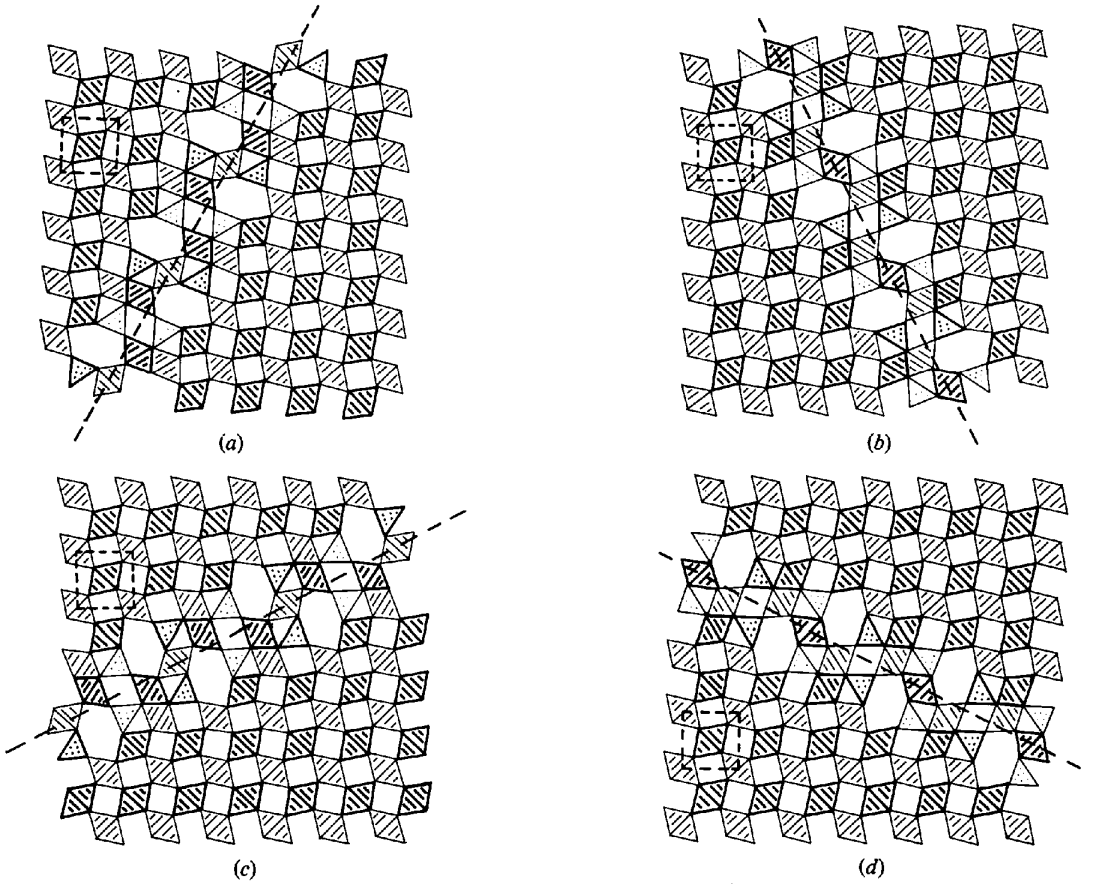

Fig. 2. (*a*), (*b*), (*c*), (*d*) The four crystallographically equivalent $\{210\}\langle 0\frac{1}{2}0\rangle$ defect-pair structures. Note location of defect orientation relative to rutile axes (small square).

projection). However, if the junction itself contains a four- or twofold axis then the multiplicity reduces to 1 or 2 respectively. Since 26 of the 41 classes do not possess an inversion centre or vertical mirror then there are 41 + 26 physically distinct intersections. These are represented in Fig. 4. This figure, together with the symmetry factors and the sequential labelling scheme given in Table 2, provides a basis for the classification and statistical analysis of the observed intersection structures.

3. Experimental

(*a*) *Crystal growth and preparation of samples*

Weighed amounts of finely powdered MgO and TiO_2 were mixed, formed into pellets and reacted at 1473 K for 48 h. The following observations refer to the titania-rich portion of a sample having overall stoichiometry $(Ga,Ti)O_{1.925}$. In fact, the crystals selected for this study have stoichiometry more like $(Ga,Ti)O_{1.995}$, judged by the observed density of defect-pairs. This titania-rich portion may simply be relatively unreacted material, owing to the low temperature, or it may be in equilibrium with the more-gallia-rich portion $Ga_4Ti_{m-4}O_{2m-2}$ ($m \simeq 20$), which constitutes the remainder of this preparation. Thin fragments were ground under chloroform in an agate mortar and deposited onto carbon-lace support films.

Gallia-doped rutile was obtained by sprinkling finely powdered Ga_2O_3 onto one surface of a 1 mm thick (001) slice from a single-crystal rutile boule (99·8% purity, National Lead Company). This was heated in a platinum boat, in air, at 1273 K for 8 d, followed by further heating at 1773 K for 5 d. The slice was then thinned mechanically, from the undoped side, to approximately 30 μm, then finally ion-thinned from both sides.

(*b*) *Electrical optical parameters*

A Jeol-100C electron microscope, fitted with a slightly modified BLG goniometer, was operated using objective-lens pole-pieces with spherical aberration coefficient $C_s = 2{\cdot}4$ mm, focal length $f_o = 2{\cdot}2$ mm and chromatic aberration coefficient $C_c = 2{\cdot}0$ mm. Most of the micrographs were recorded using slightly defocused illumination (semi-cone angle 0·6–0·8 mrad), when the effective point-to-point resolution is limited to the range 3·2 to 3·8 Å (see Bursill & Wilson, 1977).

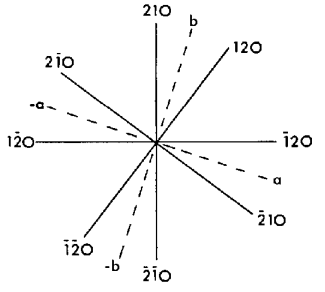

Fig. 3. Labelling scheme for intersecting $\{210\}\langle 0\frac{1}{2}0\rangle$ defect-pairs showing location relative to rutile tetragonal axes *a* and *b*.

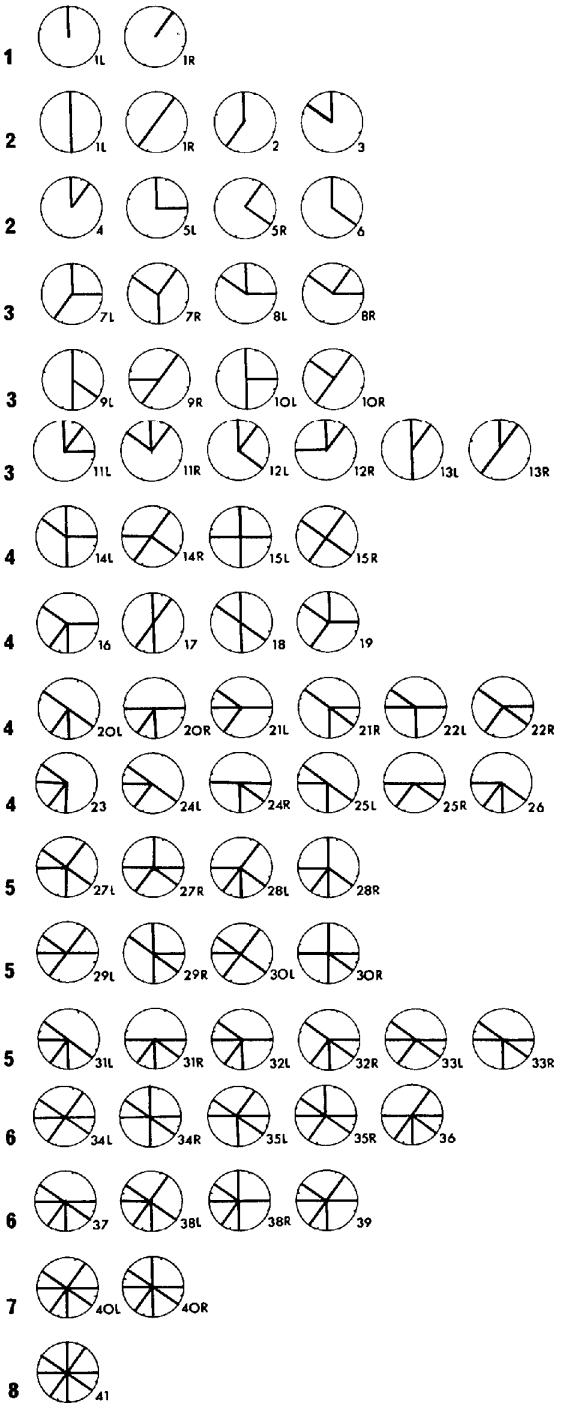

Fig. 4. Representation of the 41 intersection classes and sequential labelling scheme. *L* and *R* indicate left- and right-handed forms.

4. Observations

(*a*) Mg-*doped rutile*

Fig. 5 shows a relatively low magnification image of {210} defect-pairs in Mg-doped rutile, viewed edge-on in the [001] zone. Three of the four possible orientations occur, *i.e.* (210), (2$\bar{1}$0), (120). Note the terminating defects (*T*) and the four distinct intersections 3, 11*L*, 17 and 18. Higher-magnification prints (*e.g.* Fig. 6) reveal that the defects are in fact Ga_4TiO_4 defect-pairs (*cf.* Fig. 1*b*). The hexagonal tunnels image as large white blobs for objective-lens defocus −1000 Å. Note also the 4·6 × 4·6 Å image of the rutile subcell; this clearly does not represent the metal atoms of rutile in this projection, which should give a 3·2 × 3·2 Å net. Broad dark bands parallel to the defect image and some of the defect-image detail are due to so-called reflex image formation since the effective objective aperture includes strong rutile reflections (for detailed interpretation see Bursill & Barry, 1977).

Fig. 7 shows a second example exhibiting all four {210} orientations with a wide variety of intersections, labelled according to the code in Fig. 4. Note that a number of defects terminate just prior to possible intersections (*T'*). The enlargement (Fig. 8) shows detail for three orthogonal junctions. Note the different contrast

Table 2. *Classification and observed frequency of* {210} *intersection structures in doped rutile*

Number of elements *n*	Serial number		Symmetry reduction factor	Burger's vector of stair-rod dislocation	Observed frequency Mg *L*	Mg *R*	Ga *L*	Ga *R*
1	1*L*	1*R*	4 4	$[0\frac{1}{2}0]$				
2	1*L*	1*R*	2 2	$[0\frac{1}{2}0]$				
	2		4	$[\frac{1}{2}\bar{\frac{1}{2}}0]$	0	0	0	0
	3		4	0	5		13	
	4		4	$[\frac{1}{2}\frac{1}{2}0]$			2	
	5*L*	5*R*	4 4	$[\frac{1}{2}\frac{1}{2}0]$	0	1	4	4
	6		4	$[0\bar{1}0]$			2	
3	7*L*	7*R*	4 4	$[\bar{1}\frac{1}{2}0]$	0	0	0	0
	8*L*	8*R*	4 4	$[\frac{1}{2}00]$	0	0	0	1
	9*L*	9*R*	4 4	$[0\frac{1}{2}0]$	1	1	26	38
	10*L*	10*R*	4 4	$[\frac{1}{2}00]$	3	1	39	33
	11*L*	11*R*	4 4	$[0\frac{1}{2}0]$	1	0	0	0
	12*L*	12*R*	4 4	$[1\frac{1}{2}0]$	0	0	2	0
	13*L*	13*R*	4 4	$[\frac{1}{2}00]$	1	2	11	21
4	14*L*	14*R*	4 4	$[\frac{1}{2}\frac{1}{2}0]$	0	0	0	0
	15*L*	15*R*	1 1	0	2	6	11	32
	16		4	$[\bar{1}\bar{1}0]$	0	0	0	0
	17		2	0	7	0	16	2
	18		2	0	4	0	13	4
	19		4	$[\bar{1}00]$	0	0	0	0
	20*L*	20*R*	4 4	$[\bar{\frac{1}{2}}\bar{\frac{1}{2}}0]$	0	0	1	3
	21*L*	21*R*	4 4	$[\bar{\frac{1}{2}}\bar{\frac{1}{2}}0]$	0	0	0	1
	22*L*	22*R*	4 4	$[0\bar{1}0]$	0	0	0	0
	23		4	$[0\bar{1}0]$	0		0	
	24*L*	24*R*	4 4	0	0	0	27	17
	25*L*	25*R*	4 4	$[\frac{1}{2}\frac{1}{2}0]$	0	0	3	1
	26		4	0	1		0	
5	27*L*	27*R*	4 4	$[1\bar{\frac{1}{2}}0]$	0	0	0	0
	28*L*	28*R*	4 4	$[\frac{1}{2}00]$	0	0	0	1
	29*L*	29*R*	4 4	$[0\bar{\frac{1}{2}}0]$	0	0	0	1
	30*L*	30*R*	4 4	$[0\frac{1}{2}0]$	0	0	5	4
	31*L*	31*R*	4 4	$[0\bar{\frac{1}{2}}0]$	0	0	0	3
	32*L*	32*R*	4 4	$[\bar{\frac{1}{2}}10]$	0	0	0	0
	33*L*	33*R*	4 4	$[\bar{\frac{1}{2}}00]$	0	0	3	3
6	34*L*	34*R*	2 2	0	0	0	0	1
	35		4	$[\frac{1}{2}\frac{1}{2}0]$	0		0	
	36		4	0	0		0	
	37		4	$[\frac{1}{2}\frac{1}{2}0]$	0		0	
	38*L*	38*R*	4 4	$[\bar{\frac{1}{2}}\bar{\frac{1}{2}}0]$	0	0	0	2
	39		4	$[0\bar{1}0]$	0		0	
7	40*L*	40*R*	4 4	$[\frac{1}{2}00]$	0	0	0	0
8	41		1	0	0	0	0	0
0	0		1	–		–		
Totals			256		25	11	178	172

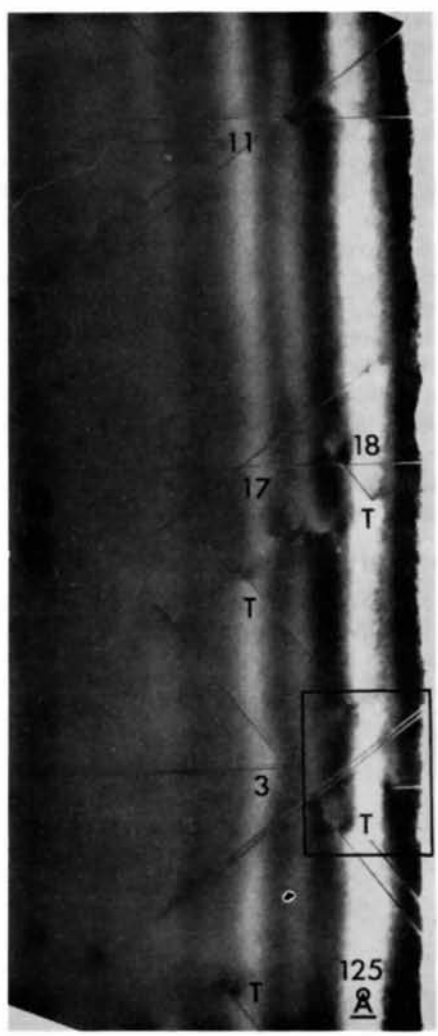

Fig. 5. Low-magnification image of {210} defect-pairs in Mg-doped rutile ([001] projection). Note the terminating defects (*T*) and the four distinct intersection classes 3, 11*L*, 17, 18.

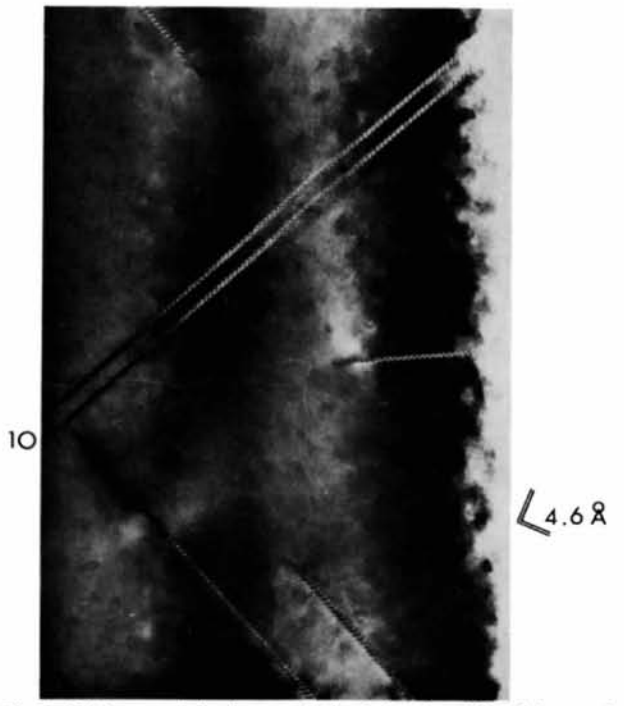

Fig. 6. Higher-resolution image of Fig. 5 showing white-blob tunnel images, objective-lens defocus approximately −1000 Å. Two components of the displacement vector may be read off by sighting along the 4·6 × 4·6 Å fringes indicating the rutile unit cell.

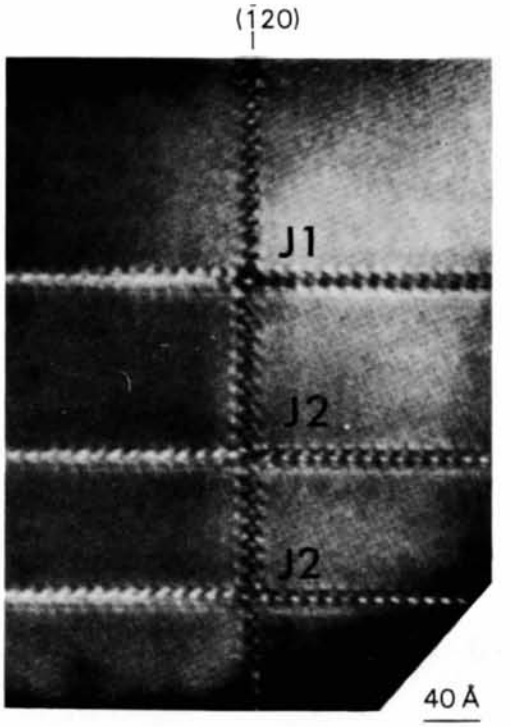

Fig. 8. Enlargement of part of Fig. 7 showing three orthogonal junctions of class 15. *J*1 and *J*2 show different contrast and note apparent shift of the (1̄20) component.

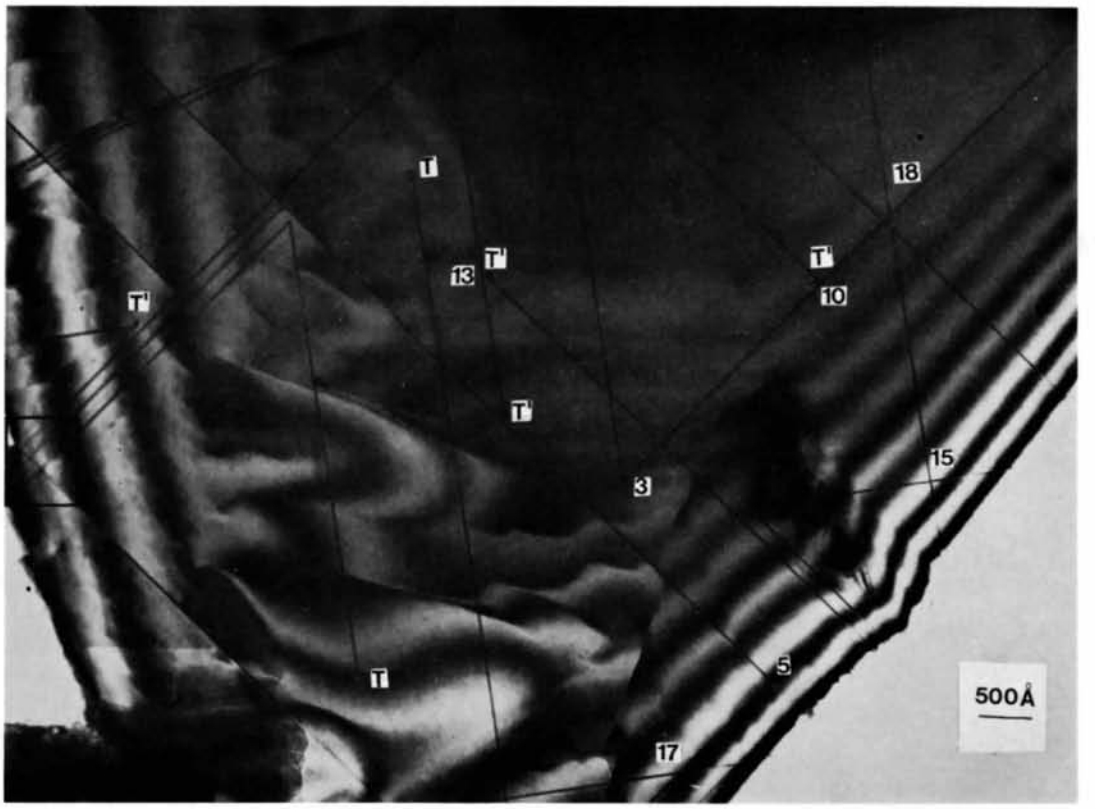

Fig. 7. Further examples of intersections in Mg-doped rutile; note a number of defect-pairs terminating just short of possible intersections (*T'*). Classes 3, 5, 13, 15, 17 and 18 are labelled.

at $J1$ and $J2$ and the apparent small shift ($\simeq 5$ Å) of the $(1\bar{2}0)$ defect-pair at each of the intersections.

(*b*) Ga-*doped rutile*

Fig. 9 shows an overall view (low magnification) of the ion-thinned Ga-doped slice. A maze of intersections and junctions may be seen. Enlargements of Fig. 9 were used to identify and label 350 of these. The appearance of T' terminations in Fig. 7 suggests that these may also occur in Fig. 9. Since the latter has insufficient resolution to resolve these they have been labelled as normal intersections for inclusion in the statistical analysis. Table 2 lists the observed frequency distribution among the possible classes, for both the Mg- and Ga-doped rutile.

Spotty background contrast in Fig. 9 made high-resolution studies of the ion-thinned specimen difficult. This is presumably due to ion damage. However, some fragments from the rutile slice, before ion-thinning, were examined. In addition to the defect intersections, steps (S in Fig. 10*a*) in widely spaced single $(210)[\frac{1}{2}\frac{1}{2}\frac{1}{2}]$ CSP and a hair-pin bend (U in Fig. 10*b*) were found. Note also the 'V'-shaped 'slip-stream' type contrast associated with three of the CSP in Fig. 10(*a*), as they approach the crystal edge. One defect appears to swing around through 90° before intersecting with its neighbour. These manoeuvres may be associated with the splitting of defect pairs and the formation of high-m $Ga_mTi_{m-4}O_{2m-1}$ ordered structures.

5. Discussion

We note from Table 2 that 25 of the possible 41 intersection classes occur; of these only eight account for 87% of the observations. Now the energetics of intersection structures should be largely determined by the magnitude of the stair-rod dislocation Burger's

Fig. 9. Low-magnification image showing intersections in ion-thinned Ga-doped rutile. Note the absence of terminations (*cf.* T in Fig. 5) and the presence of some lamellae (broad dark bands). Altogether 350 intersections were identified and classified using Fig. 4 (see Table 2).

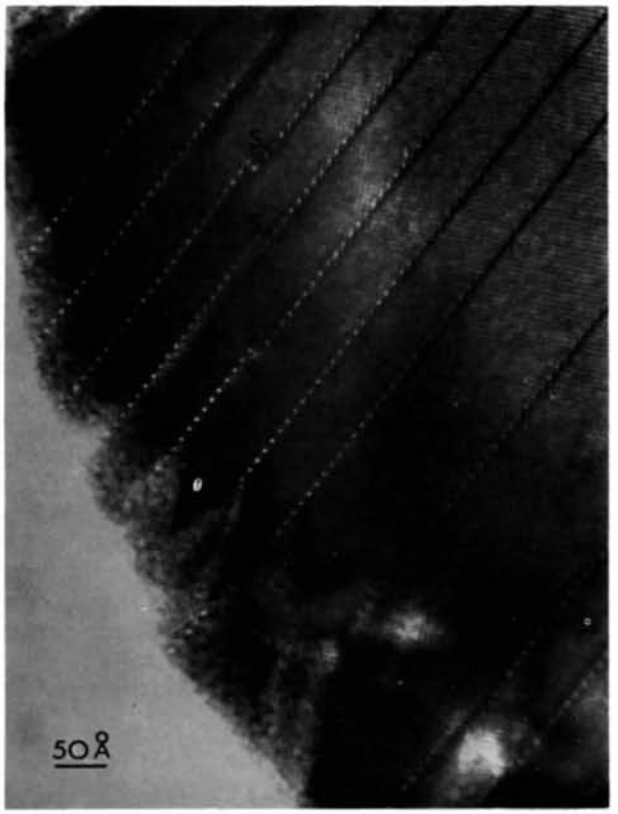

(*a*)

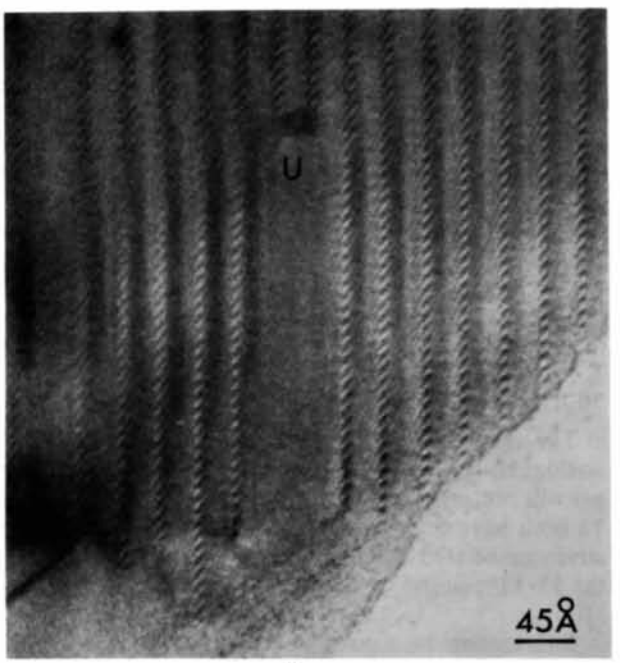

(*b*)

Fig. 10. (*a*) High-resolution image showing steps (*S*) in single (210)[$\frac{1}{2}\frac{1}{2}\frac{1}{2}$] CSP in Ga-doped rutile. A 'V' shaped region of lighter contrast resembling a 'slip stream' appears where two of the CSP approach the surface. Another CSP appears to swing through 90° before intersecting its neighbour. (*b*) A 'U' turn or hairpin bend in Ga-doped rutile, within a lamella of widely spaced CSP.

vector required to maintain continuity of the host lattice around the intersection. This vector **b** is given by

$$\mathbf{b} = \sum_{i=1}^{n} \mathbf{R}_i, \tag{1}$$

where $\mathbf{R}_i$ is the displacement vector of the *i*th defect-pair contributing to the junction and n is the total number of elements ($1 \leq n \leq 8$). Clearly, the intersection will have minimum strain energy for $\mathbf{b} = 0$. The Burger's vector is listed in Table 2 for each intersection class. There are six types: $\mathbf{b}_1 = 0$, $\mathbf{b}_2 = \langle 0\frac{1}{2}0\rangle$, $\mathbf{b}_3 = \langle \frac{1}{2}\frac{1}{2}0\rangle$, $\mathbf{b}_4 = \langle 100\rangle$, $\mathbf{b}_5 = \langle 1\frac{1}{2}0\rangle$ and $\mathbf{b}_6 = \langle 110\rangle$. Further higher-energy vectors may be obtained by adding a lattice vector to these. Note that $\mathbf{b}_2$ is identical to the Burger's vector of the partial dislocation terminating a defect-pair. Analysis of high-resolution images of such a termination yielded an atomic model of the dislocation-core structure and a mechanism for the growth of Ga_4TiO_8 defect-pairs, involving ion-exchange ($4Ga^{3+} \rightleftharpoons 3Ti^{4+}$) at the dislocation without long-range diffusion of oxygen or vacancies (Stone & Bursill, 1977). The dislocation model is reproduced for convenience in Fig. 1(*c*). Burger's vectors $\mathbf{b}_3$ to $\mathbf{b}_6$ have not been observed to operate as slip vectors in rutile; they have large energies and may be expected to dissociate into partials according to

$$\langle \tfrac{1}{2}\tfrac{1}{2}0\rangle = \langle \tfrac{1}{2}00\rangle + \langle 0\tfrac{1}{2}0\rangle; \langle 100\rangle = \langle \tfrac{1}{2}00\rangle + \langle \tfrac{1}{2}00\rangle; \textit{etc.} \tag{2}$$

We note that $b = 0$ for all 'crossed' or '×' intersections since the contributing elements always occur with antiparallel pairs of vectors. For 'V' bends **b** may be 0 (as in class 3), for antiparallel vectors, or $\langle \frac{1}{2}\frac{1}{2}0\rangle$ (as in class 4). Finally, all 'T' junctions have $\mathbf{b}_1 = \langle 0\frac{1}{2}0\rangle$.

In fact, 95·6% of the observed intersections have $\mathbf{b}_1$ or $\mathbf{b}_2$ (see Table 2); 3·4% have $\mathbf{b}_3$, and the remainder have $\mathbf{b}_4$ and $\mathbf{b}_5$ (each 0·5%). Thus, as expected, $\mathbf{b} = 0$ or $\langle 0\frac{1}{2}0\rangle$ predominate. This would not be the case for a set of random intersections, implying that the texture observed in Fig. 9 resulted after some rearrangement of the intersections and a considerable approach towards an equilibrium network. It is impossible to say whether this is stable or metastable. The Ga-doped specimen shows a relatively large number of triple and quadruple junctions compared with Mg-doped rutile, despite the poorer statistics. There are also many more terminating defect-pairs in the latter (12 in Fig. 5 compared with only one in Fig. 9), implying a closer approach to equilibrium for the Ga-doped specimen. However, such a conclusion requires that the mean dopant concentrations be the same in the two preparations and we cannot establish this. The existence of one defect (circled in Fig. 9) stepped onto a mean plane which is not of {210} type suggests that rearrangement is still occurring, even after 13 d reaction. The occurrence of lamellae of {210} defects, unresolved in Fig. 9 but

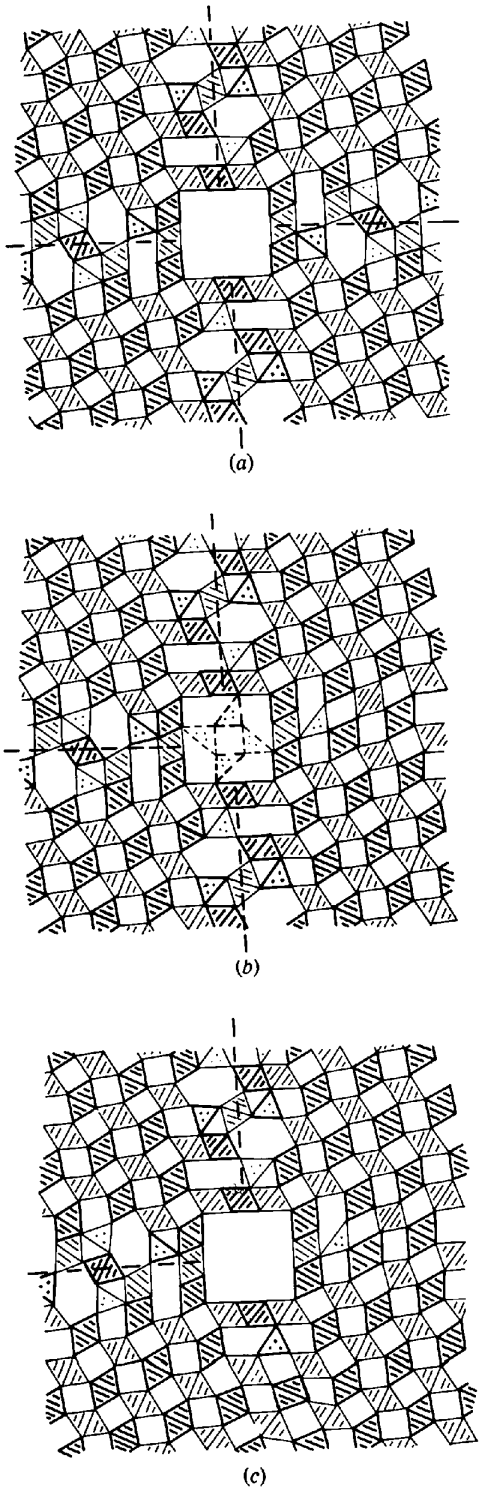

Fig. 11. Structural models for intersection classes (*a*) 15, (*b*) 10 and (*c*) 5. The crossed intersection 15 requires four orthogonal strips of triple edge-sharing of octahedra, forming a large tunnel having square cross section. Classes 10 and 5 follow from 15 by drawing in the stair-rod dislocations, replacing one and two {210} elements in turn. A long-range strain is set up but there are no new polyhedral linkages.

possibly similar to Fig. 10(*a*), suggests that aggregation occurs after a reasonably stable intersection network is established.

We now give some examples of model structures proposed for the common intersections.

Orthogonal intersections 15, 10 *and* 5

These all occur, with frequency 10 > 15 > 5. The crossed intersection 15 requires four orthogonal strips of three edge-shared octahedra (Bursill, 1979*a*). These link to form an extraordinarily large square tunnel (Fig. 11*a*). Each triple edge-shared strip may be regarded as the termination of the corresponding {210} defect-pair (*cf.* Fig. 1*c*). Intersections 10 and 5 may be derived from 15 by inserting stair-rod dislocations having Burger's vectors $[0\frac{1}{2}0]$ and $[\frac{1}{2}\frac{1}{2}0]$ respectively. These take on the almost trivial structural form shown in Fig. 11(*b*,*c*). Only very slight changes are required in the polyhedral linkages and the dislocation core involves only elements of the β-gallia structure, as already exist in the Ga_4TiO_8 defect-pairs. The same large square tunnel occurs in each case; this may be empty or filled; for example, a column of β-gallia-type tetrahedra are dotted in Fig. 11(*b*).

53·13° *intersections* 18, 9, 6 *and* 3

The crossed 53·13° (18) intersection is given in Fig. 12(*a*). Ga_4TiO_8 defect-pairs interpenetrate with only slight disturbance of the normal hexagonal tunnel structure. Only two triple edge-shared strips are required and no new structural elements occur. The 'Y' junction (9), shown in Fig. 12(*b*), involves one triple edge-shared strip and since $\mathbf{b} = 0$ this is more frequent than 18. Intersection 6, Fig. 12(*c*), is more complex, with two edge-shared strips, and this has much lower frequency. Intersection 3, Fig. 12(*d*), a 'V' junction, has $\mathbf{b} = 0$ but it requires two edge-shared strips and is found with frequency intermediate between 18 and 6.

36·87° *intersections* 17 *and* 13

The structure models are similar to the 53·13° analogues, but since they have much lower frequency we will not reproduce them here. Even though 17 and 18 both have $\mathbf{b} = 0$ it appears that there may be more strain associated with the 36·87° intersection than for the 53·13°; similarly for 13 and 9, which both have $\mathbf{b} = [\frac{1}{2}00]$.

Intersection 24, a quadruple junction, has a relatively high frequency (Table 2), which presumably arises because it has $\mathbf{b} = 0$. This and other complex intersection structures may be readily derived by compounding the above models.

It is interesting to note that, whereas there are large fluctuations in the distribution between left- and right-

handed forms in the same class, overall the distribution is even-handed.

Clearly, further careful electron optical study of the intersection structures is necessary to determine whether the tunnels are filled or empty, or whether the apparent shifts in Fig. 8 are artifacts, because of the details of the electron optical conditions, or represent further complications in structure. Such a study is not trivial, requiring through-focal-series of images and N-beam multislice calculations for comparison with experiment. The low probability of finding an example of a chosen class in a sufficiently thin area of crystal means that we do not contemplate such a systematic study. Structural models for steps in CSP oriented parallel to the incident beam, such as shown above in Fig. 10(*a*), have already been given (Stone & Bursill, 1977). The 'U' turn (Fig. 10*b*) simply consists of two class 5 junctions.

5. Conclusion

It is important to realize that new structure-building elements arise at defect intersections. The large tunnels

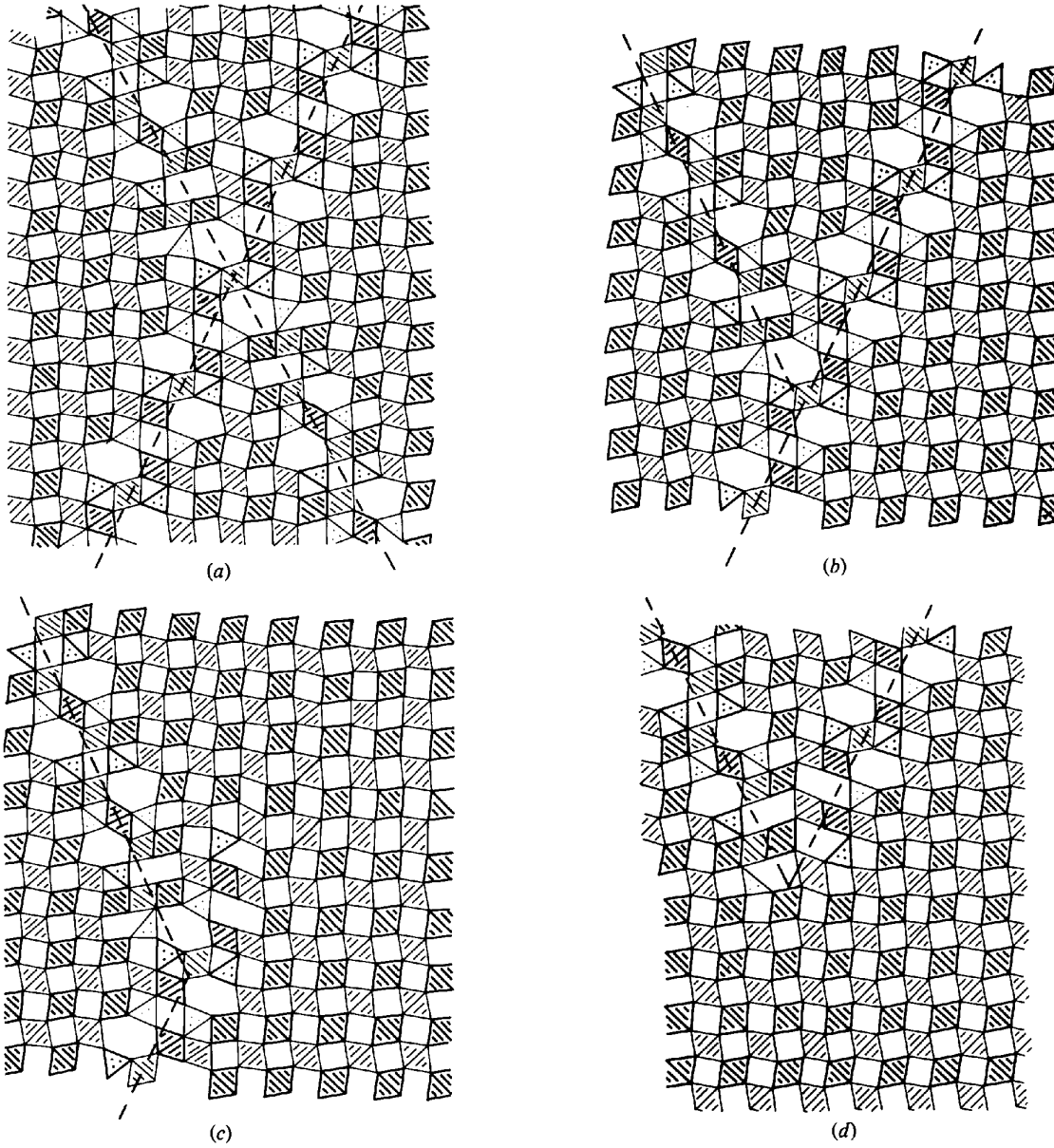

Fig. 12. Structural models for intersections (*a*) 18, (*b*) 9, (*c*) 6 and (*d*) 3. Two edge-shared strips are required for 18, 16 and 3, but only one for 9. No large tunnels are produced.

shown in Fig. 11 are interesting. Their formation should be enhanced by suitable doping, for example with Ba^{2+} or similar disposable ions, in addition to the Ga, Mg or Al ions required to produce {210} defect-pairs. A systematic study of the preparative conditions is required. The intersection structures may act as nuclei for phase transformations or transitions. The former has been observed for the low- to high-temperature transformation in the Fe–Ti–O and Cr–Ti–O systems (Bursill, Netherway & Grey, 1978), where the intersections aggregate and order producing a high-temperature structure having minimum elastic strain energy.

The observation that some defect-pairs terminate just short of possible intersections (Fig. 7) suggests that some of the intersections require higher thermodynamic driving force. A study of the mobility of such structures (experimentally using a high-temperature goniometer and theoretically, in terms of atomic-diffusion mechanisms and energies of formation, interaction and migration) should prove interesting. However, even at this stage, it should be appreciated that such energy terms will largely determine the kinetics of the reaction between rutile and its dopants. Similar intersection structures have been observed in TiO_x (Bursill, Hyde, Terasaki & Watanabe, 1969); here there are numerous possibilities, with eight {132} and four {101} contributing. These must make significant contributions to the very large hysteresis between reduction and oxidation paths found by thermodynamic studies (Merritt & Hyde, 1973).

This work was financially supported by the Australian Research Grants committee and the University of Melbourne. The author thanks Mr G. G. Stone for preparing the ion-thinned specimen.

References

BURSILL, L. A. (1979*a*). *Acta Cryst.* B**35**, 530–538.

BURSILL, L. A. (1979*b*). *Acta Cryst.* Submitted.

BURSILL, L. A. & BARRY, J. C. (1977). *Philos. Mag.* **36**, 497–510.

BURSILL, L. A., HYDE, B. G., TERASAKI, O. & WATANABE, D. (1969). *Philos. Mag.* **20**, 347–359.

BURSILL, L. A. & NETHERWAY, D. J. (1979). *Acta Cryst.* Submitted.

BURSILL, L. A., NETHERWAY, D. J. & GREY, I. E. (1978). *Nature (London)*, **272**, 405–410.

BURSILL, L. A. & STONE, G. G. (1975). *Philos. Mag.* **32**, 1151–1158.

BURSILL, L. A. & STONE, G. G. (1979*a*). *Acta Cryst.* Submitted.

BURSILL, L. A. & STONE, G. G. (1979*b*). *Philos. Mag.* Submitted.

BURSILL, L. A. & WILSON, A. R. (1977). *Acta Cryst.* A**33**, 672–676.

GIBB, R. M. & ANDERSON, J. S. (1972). *J. Solid State Chem.* **5**, 212–225.

LLOYD, D. J., GREY, I. E. & BURSILL, L. A. (1976). *Acta Cryst.* B**32**, 1756–1761.

MERRITT, R. R. & HYDE, B. G. (1973). *Philos. Trans. R. Soc. London. Ser. A*, **274**, 627–661.

STONE, G. G. & BURSILL, L. A. (1977). *Philos. Mag.* **35**, 1397–1412.

Acta Cryst. (1979). A**35**, 458–462

X–N and *X–X* ($1s^2$ Core) Maps for Cyanuric Acid

BY A. KUTOGLU AND C. SCHERINGER

Institut für Mineralogie der Universität Marburg, D 3550 Marburg, Federal Republic of Germany

(*Received* 4 *December* 1978; *accepted* 18 *January* 1979)

Abstract

X–N maps and *X–X* ($1s^2$ core parameter) maps of cyanuric acid, $C_3H_3N_3O_3$, at 100 K are presented. The differences in scale and in the atomic parameters have large effects ($\leq 0{\cdot}4$ e Å^{-3}) on the difference density at the nuclei but smaller effects ($\leq 0{\cdot}15$ e Å^{-3}) on the bond density distributions. In particular, the density distribution around the O atoms, where polarization is likely to occur, is different in the two types of maps. It is concluded that, in these regions, the *X–N* maps yield the more reliable results.

0567-7394/79/030458-05$01.00 © 1979 International Union of Crystallography

Introduction

From a previously refined model of the electron density distribution in cyanuric acid (100 K X-ray data of Verschoor & Keulen, 1971), the positional and thermal parameters of the $1s^2$ atomic cores were determined (Kutoglu & Hellner, 1978). *X–X*($1s^2$) and *X–N* maps were calculated with the neutron parameters of Coppens & Vos (1971). Owing to an error in the data transmission of the form-factor curve of the O atom, both maps were falsified. The corrected maps are given in this paper (Figs. 1 and 2).